Modeling of the saturated Ni-like silver x-ray laser

D. Benredjem, C. Möller, and J. Dubau
LIXAM, Université Paris-Sud, Centre d'Orsay, Bâtiment 350, 91405 Orsay, France

J. Kuba* and R. F. Smith
Lawrence Livermore National Laboratory, Livermore, California 94550, USA

C. Mossé
PIIM, Université de Provence, Centre de Saint-Jérôme, 13397 Marseille, France
(Received 4 October 2004; published 26 July 2005)

This paper reports on the modeling of the Ni-like silver transient x-ray laser at the wavelength of 13.9 nm. Time-dependent populations and gain are calculated consistently with the output intensity. Two-dimensional refraction, i.e., in the direction of the driving laser and parallel to the slab target surface, is modeled by a ray trace code which is a postprocessor of a hydrodynamic code. Temperatures and electron-density variations are given by the hydrocode. Our calculations show that interaction of the x-ray laser field with the amplifying medium, and refraction, affect the output intensity and reduce the gain values by a large factor: from many hundreds per cm, as predicted by collisional-radiative models ignoring the above interaction, to one hundred per cm, at most.

DOI: 10.1103/PhysRevA.72.013821 PACS number(s): 42.55.Vc, 42.15.Dp

I. INTRODUCTION

In the standard quasi-steady-state (QSS) scheme of x-ray lasers (XRLs) pumped by intense laser pulses, a solid target is irradiated by one or several low-energy prepulses followed by a relatively long pulse (100–600 ps). The pulse produces a nearly cylindrical plasma column and creates population inversion. Gain-length products $\sim$15 are routinely reached with pump energies of typically 100–1000 J [1,2]. Such saturated XRLs are robust and adapted to many applications.

During the last decade considerable progress has been made in the reduction of the necessary pump energy in order to realize small size driving lasers. The energy requirements were recently dramatically reduced to a few joules after the development of a promising new scheme [3]. This so-called transient scheme consists in a two-stage target irradiation. First, a low intensity pulse of 300–600-ps duration creates the plasma with a large proportion of the desired ion species, i.e., Ne like or Ni like. Then, a high-intensity picosecond pulse heats the preformed plasma. As a result, transient population inversions are obtained due to collisions between free electrons and ions.

Since the plasma is short lived ($<$10 ps) compared with the photon propagation time in the amplifying medium ($\sim$33 ps for a 1-cm target), the short pulse must heat the plasma only locally and make the gain region travel at the velocity of XRL photons. This is known as the traveling-wave (TW) irradiation geometry. The beneficial effect of the TW was observed by Tallents *et al.* [4] and, subsequently, the increase of the XRL output intensity was measured to be a factor of 300–400, compared with the non-TW irradiation, for a 400-fs heating pulse. With the TW, a gain of 33 cm^{-1} with a saturation length of 3.8 mm was observed during this experiment. The combination of short duration high-gain and TW irradiation results in $\sim$ 2-ps XRL pulses for the $4d-4p$ Ni-like silver transition at 13.9 nm, which are the shortest XRL pulses observed up to now [5].

The transient XRL experiments, including those on Ni-like Ag, were simulated numerically by several authors [6–8]. Results are in qualitatively good agreement with experiments. However, calculated gains are one order of magnitude larger than measured gains.

In this paper, we extend the work presented in Ref. [7], by studying the propagation of the Ni-like silver laser beam, at the wavelength of 13.9 nm. Two approaches are investigated. In the first-one a two-dimensional (2D) ray-trace code working as a postprocessor with the hydroatomic code EHYBRID [9] is used to model the experiment carried out in 2000 at the Rutherford Appleton Laboratory (RAL) [5]. The effect of saturation on gain is taken into account through a simple relation. The second approach is based on the Maxwell-Bloch formalism and describes the effect of saturation on populations more rigorously.

II. 2D RAY TRACING

Owing to the pump geometry currently used, the refraction of the XRL beam occurs in the plane perpendicular to the target surface. Electron-density gradients are steeper in transient XRLs than in the QSS scheme [6,7], and hence refraction becomes a substantial issue, dramatically limiting amplification.

Ray tracing was studied both analytically and numerically in the QSS scheme by several authors [10,11]. Chilla and Rocca [12] have found simple analytical solutions for opti-

*Present address: Faculty of Nuclear Sciences and Physical Engineering, Czech Technical University in Prague, Brehova 7, Praha, Czech Republic.

mum amplification in capillary discharge laser plasmas. Ray trajectories were also calculated analytically by Kuba *et al.* [13] and numerically by Shlyaptsev *et al.* [14] for a transient XRL. In analytical studies (see, e.g., Refs. [10,11]), refraction is investigated by assuming that the electron-density gradient occurs only in the direction of the driving laser beam, i.e., the gradient in directions parallel to the target surface is neglected. A linear electron-density profile is often used because of its simplicity. However, its real physical application is limited: all beams, at any distance from the target, always remain parallel, due to the constant gradient. London [10] has obtained an analytical solution for a parabolic electron-density profile. While this profile shows a qualitative agreement with experimental observations in XRL plasmas from exploding foil targets, it is not realistic when one uses slab targets. In fact, for such a profile the gradient rises with distance from the target. When slab targets are involved, it is preferable to use exponential profiles [11], which are predicted by analytical considerations on isothermal plasma expansion into vacuum. Such profiles are also in good agreement with simulations, see, e.g., Ref. [14]. In this work, we develop a numerical approach which accounts for refraction in the two directions perpendicular to the direction of amplification. The ray-trace code is constructed as a postprocessor of the EHYBRID code.

A. Gain calculations

The first step of our modeling of the RAL experiment concerns gain variation with time and distance to target. We have used the hydrodynamic-atomic package EHYBRID developed by G. J. Pert [9] to understand the evolution of the lasing material. This code accounts for many physical processes (pump-laser energy deposition, hydrodynamic motion, electronic thermal conduction, and ion-electron thermalization) which are coupled with the atomic physics of the lasing ion. The model is 1.5D and the fluid expansion occurs in the direction of the driving laser with cells (294 Lagrangian cells) that are assumed to be laterally isothermal: the transverse expansion is assumed to be self-similar. The calculation of the ionization balance, and in particular the abundance of nickellike ions, is very important in these calculations. In each cell, the ionization kinetics is calculated using a collisional-radiative (CR) model which represents the most sophisticated treatment available of time-dependent atomic physics in plasmas. Electron-ion collision (excitation, deexcitation, and ionization) and recombination (three-body, radiative, and dielectronic) processes are included in the coupled rate equations for each ionic level. Radiative losses are taken into account. Radiation trapping is taken into account through escape factors that can be controlled in the input file. A great challenge in EHYBRID is the absence of radiative processes involving the x-ray line, such as absorption and induced emission. In fact, EHYBRID does not account for line propagation and saturation effects.

The ionization rate of Golden *et al.* [15] is implemented, with three-body recombination calculated from the detailed inverse balance. Processes such as excitation autoionization and inner-shell ionization are not considered, but this level of detail for the lasing ion is found to produce good agreement with experiment. However, computational limitations mean that more approximate descriptions must be implemented for the other ion stages. In the data set for silver, all ion stages, except the nickel-like stage, are treated by a simple hydrogenic screened model or a two-level model based on a modified form of Griem's model [16].

Absorption of the driving laser energy is due to inverse bremsstrahlung. The inverse bremsstrahlung coefficient is calculated for the propagation of the laser pulse towards the target surface and for reflection of the laser pulse away from the critical surface. Higher-field modifications of this coefficient are not included. Resonant absorption is modeled by assuming a 30% dump of the laser energy reaching the critical surface. The thermal conductivity for both ions and electrons is given by the classical Spitzer-Harm expression [17]. As this formula is valid only if the mean free path of electrons remains small compared to the typical temperature gradient dimensions, the thermal conductivity is subject to an empirical flux limit of $f=0.1$, as usual in this type of code. There are some modifications to this parameter in the low-temperature, solid-density region (applicable to low-level prepulses). Atomic physics, hydrodynamics, and transport within the plasma are solved self-consistently through a solution of the electron energy balance.

In a previous work [7], we have shown the evolution, with time and distance from target surface, of the free-electron density, average ionization stage, bremsstrahlung emission, as well as of the fractional abundances of the various ionic stages.

The atomic database of the nickel-like stage consists of a set of 272 excited levels including all levels of the $n=4-5$ manifolds, and averaged contributions from the $n=6-8$ levels. Oscillator strengths for all transitions in the $n=4-8$ manifolds were calculated with a multiconfigurational Dirac-Fock code [18]. Electron-ion collision strengths for all transitions within the $n=4$ manifold were calculated at LULI (Ecole Polytechnique, France) by using the code HULLAC [19]. The calculations allow for one vacancy in the $n=3$ shell. To obtain reliable excitation and deexcitation rates, the collision strengths were calculated for ten electron energies. Rather than using the standard fitting procedure involving d coefficients [20], which is not appropriate for this ionic stage, we have added a subroutine into EHYBRID, which provides all the rates for each electron density and temperature. Basically, this subroutine calculates an effective collision strength with the help of the Laguerre-Gauss method [21].

Figure 1 shows the gain on the $4d^1S_0-4p^1P_1$ line (13.9 nm), as a function of time and distance from the target surface. The long pulse full width at half maximum (FWHM) is 300 ps and the short pulse (FWHM=1.3 ps) occurs with a 200-ps peak-to-peak delay. Two distinct regions are predicted. When the short pulse is turned on, a large gain region (>500 cm^{-1}) emerges with small dimensions both in space (within 25–30 μm from the target surface) and time (<2 ps at FWHM). When the laser is turned off, a large plateau with gains <400 cm^{-1} extending out to ~ 50 μm is observed. These results are similar to those of Yan *et al.* [8].

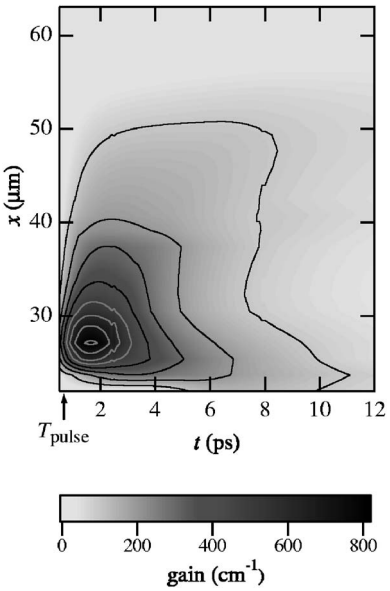

FIG. 1. Local gain on the 0-1 line in Ni-like silver, obtained by modeling the experiment at RAL [5] with EHYBRID. Contour curves are drawn for gain coefficient values 100–800 cm^{-1}. t and T_{pulse} are, respectively, the time after the onset and the time of the maximum of the second pulse. x is the distance from the target surface.

B. 2D ray tracing

The propagation of transverse waves in a neutral plasma is described by the vector wave equation [22]:

$$\left(\Delta - \frac{1}{c^2}\frac{\partial^2}{\partial t^2} - \frac{\omega_p^2}{c^2}\right)\mathbf{E} = \mathbf{0}, \tag{1}$$

where $\mathbf{E}$ is the electric field and ω_p the electron plasma frequency. The third term, which is proportional to the time derivative of the free-electron current density, gives rise to refraction and diffraction. In this work, electron-ion collisions, which are responsible for collisional damping or inverse bremsstrahlung are ignored. A beam trajectory in a medium with electron-density gradient ∇n_e is then described by the following equation (see, for example, Ref. [23]):

$$\frac{d}{ds}\left(n\frac{d\mathbf{r}}{ds}\right) = \nabla n(\mathbf{r}), \tag{2}$$

where $ds=(dx^2+dy^2+dz^2)^{1/2}$ is the path element and n the refraction index. This equation is valid in the geometric optics approximation, when the Fresnel number is large and the ratio between the gain factor and the refraction coefficient is small [24]. We assume that the values of s are discrete and equally spaced. We set $s_0=0$, $s_1=\Delta s$, $s_2=s_1+\Delta s, \ldots s_{i+1}=s_i+\Delta s, \ldots$, $s_N=s_{N-1}+\Delta s$, where $s_N=L$ is the path length.

The refraction index is given in terms of the electron density by the well-known relation

$$n = \sqrt{1-\frac{n_e}{n_c}}, \tag{3}$$

where n_c is the critical density. In our Cartesian coordinates system, the y and z axes are parallel to the target surface. Moreover, z is taken to be the direction of amplification, in the absence of refraction. The x axis is orthogonal to the target surface. EHYBRID gives the electron density as a function of the coordinate x and time, $\tilde{n}_e(x,t)$. We assume that the variation with the coordinate y is represented by a Gaussian profile, i.e.,

$$n_e(x,y,t) = \tilde{n}_e(x,t)\exp\left(-4\ln(2)\frac{y^2}{r_0^2}\right), \tag{4}$$

where r_0 is the focal line half width. In the paraxial approximation, $d/ds \approx d/dz$ and Eqs. (2) and (3) yield

$$\frac{d^2x}{dz^2} = \frac{d\alpha}{dz} = -\frac{1}{2n_c}\frac{\partial n_e}{\partial x}, \tag{5}$$

$$\frac{d^2y}{dz^2} = \frac{d\beta}{dz} = -\frac{1}{2n_c}\frac{\partial n_e}{\partial y}, \tag{6}$$

where $\alpha(\beta)$ is the angle between the z axis and the projection of the wave vector on the $xz(yz)$ plane. For an initial data set $(t_0, x_0, y_0, z_0, \alpha_0, \beta_0)$, Eqs. (5) and (6) give x, y, α, and β as functions of z or t. The intensity is given by the following relation, which describes the small-signal regime as well as the saturation regime. For a propagation length s, $s_{i-1} \leqslant s \leqslant s_i$, we have

$$I(s) = \frac{j_i}{G_i}\exp[G_i(s-s_{i-1})-1] + I(s_{i-1})\exp[G_i(s-s_{i-1})], \tag{7}$$

where the first contribution in the right-hand side accounts for the amplification of the radiation emitted in the interval $[s_{i-1}, s_i]$, while the second describes the amplification, in the same interval, of the radiation emerging from the preceding segment: $[s_{i-2}, s_{i-1}]$. The emissivity j and gain coefficient G are given by

$$j = N_u h\nu_0 \frac{r^2}{4\pi L^2}A_{ul}, \quad G = \frac{\tilde{G}}{1+\frac{I}{I_{sat}}}. \tag{8}$$

The emissivity is generally assumed to be homogeneous along the z axis. It depends on the population density of the upper level N_u, the radius r of the output region, the length L of the plasma column, and the Einstein coefficient for spontaneous emission between the two lasing levels. Since the time interval for the hydrodynamic output is fixed to 0.1 ps, the density gradient will vary during the propagation of the rays over a plasma length of typically 5 mm. The above equations allow a fast calculation of the intensity with refraction taken into account. The small-signal gain $\tilde{G}$ and saturation intensity I_{sat} are given by EHYBRID.

Figure 2 shows the intensity of the XRL beam as a function of x and y, for $L=5$ mm. One million rays are launched at three different times. The values of the angles α_0 and β_0 range from −5 to 5 mrad, with a 0.5-mrad step. Negative values of α_0 involve rays launched towards the target surface. The most intense XRL beam is obtained for rays launched at the time of peak gain T_{peak}, predicted by EHYBRID. It exits the plasma at a distance of 50 μm from the

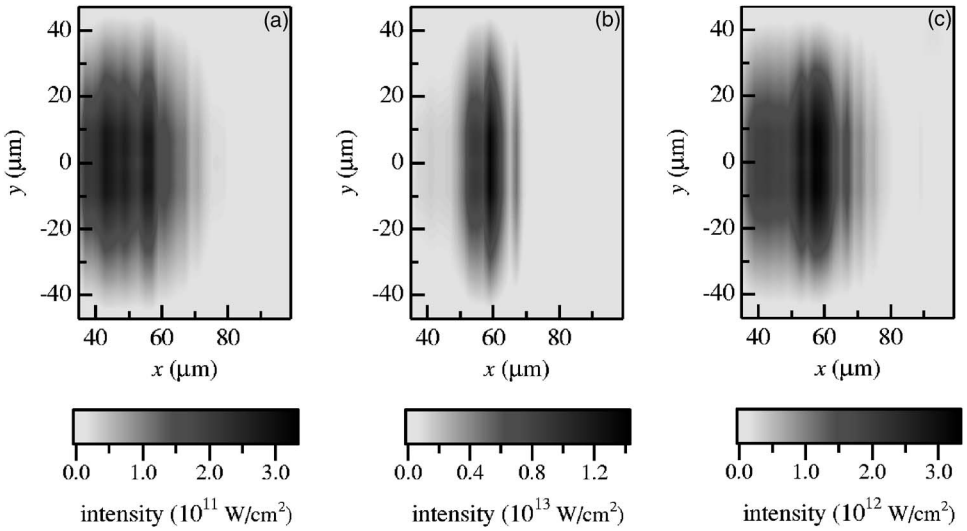

FIG. 2. Near-field image obtained for a propagation length of 5 mm in the plasma. Rays are launched (a) 1 ps before T_{gain}, the time of peak gain predicted by EHYBRID ($T_{gain}=T_{pulse}+0.85$ ps), (b) at T_{gain}, (c) 1 ps after T_{gain}. The ray-trace code was used in the conditions of the experiment performed at RAL [5].

target surface. This approach overestimates the output intensity because the saturation effect on gain is treated in a crude way.

III. MAXWELL-BLOCH APPROACH OF SATURATION AND REFRACTION

Let us account for the effect of bound electrons in the propagation of the electric field. Maxwell's equation becomes

$$\left(\Delta - \frac{1}{c^2}\frac{\partial^2}{\partial t^2} - \frac{\omega_p^2}{c^2}\right)\mathbf{E} = \frac{1}{\epsilon_0 c^2}\frac{\partial^2}{\partial t^2}\mathbf{P}. \tag{9}$$

The right-hand side of the above equation involves the atomic polarization $\mathbf{P}$ which produces spontaneous and stimulated emission and absorption. The polarization is given by $\mathbf{P}=\mathrm{Tr}(\rho\mathbf{d})$, where ρ is the density operator and $\mathbf{d}$ the atomic electric dipole. These two quantities are related by the Bloch equation:

$$i\hbar\frac{\partial\rho}{\partial t} = [H_0 - \mathbf{d}\cdot\mathbf{E}, \rho], \tag{10}$$

where H_0 is the Hamiltonian of the lasing ions, without the three radiative processes mentioned above.

As seen above, while z varies by a few mm, x and y vary by a few tens of microns. The XRL beam propagation is then, to a good approximation, parallel to the z axis (paraxial approximation). In this case, the wave vector $\mathbf{k}$ is nearly parallel to the z axis and the transverse wave is solely formed by two circularly polarized components: σ_+ and σ_-. As a result, the electric field interacts differently with the Zeeman sublevels of each lasing level, yielding different populations for the sublevels. From Eqs. (9) and (10), we can derive the population equation (see below) and the radiative transfer equation for the Zeeman sublevels [25]:

$$\frac{\mathbf{k}}{k}\cdot\nabla I_\pm(\nu,\mathbf{r},t) = j_\pm(\nu,\mathbf{r},t) + G(\nu,\mathbf{r},t)I_\pm(\nu,\mathbf{r},t), \tag{11}$$

where the emissivity in a solid angle θ, and the gain coefficient take the following forms:

$$j_\pm(\nu,\mathbf{r},t) = \frac{3\theta}{8\pi}(2J+1)A_{JJ'}h\nu\Phi_{JJ'}(\nu)\sum_M N_{JM}(\mathbf{r},t) \times \begin{pmatrix} J & 1 & J' \\ -M & \pm 1 & M\mp 1 \end{pmatrix}^2, \tag{12}$$

$$G(\nu,\mathbf{r},t) = 3\hbar k(2J+1)B_{JJ'}\Psi_{JJ'}(\nu)\sum_M [N_{JM}(\mathbf{r},t) - N_{J'M-1}(\mathbf{r},t)]\begin{pmatrix} J & 1 & J' \\ -M & 1 & M-1 \end{pmatrix}^2, \tag{13}$$

where $A_{JJ'}$ is the Einstein coefficient of spontaneous emission from the upper (J) to the lower (J') lasing level. The N's designate the population densities of the Zeeman sublevels. Φ is the lasing line emission profile and Ψ the absorption (induced emission) profile. The lasing line shape is dominated by electron impact broadening and Doppler frequency detuning (see the Appendix). Since the ion Stark broadening is negligible at any distance from the target surface, and in particular in the region of amplification, the frequency redis-

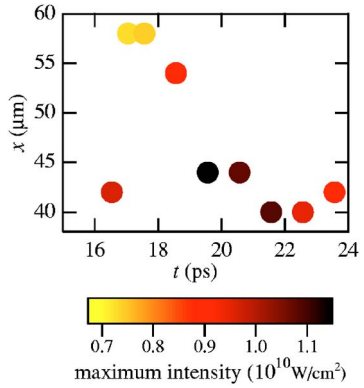

FIG. 3. (Color online) Integrated intensity of the XRL beam as a function of distance x from the target surface and time t. The propagation length $L=5$ mm. The origin of time is taken to be the maximum of the (pumping laser) short pulse.

tribution is complete. As a consequence, the two profiles are identical; see, e.g., Ref. [26].

The set of population equations consists of two groups. The first one includes all Ni-like levels except the lasing levels. To first order, these levels are insensitive to the XRL beam, and the corresponding equation does not contain an explicit dependence on the intensity of the XRL beam. The second group is formed by the Zeeman sublevels JM and $J'M'$ and the corresponding population equations are

$$\frac{\partial}{\partial t}n_{JM}(\mathbf{r},t) = r_{JM}(\mathbf{r},t) - \Gamma_{JM}(\mathbf{r},t)n_{JM}(\mathbf{r},t) - \sum_{q=\pm 1}\langle JM|d_q|J'M-q\rangle^2 \times [n_{JM}(\mathbf{r},t) - n_{J'M-q}(\mathbf{r},t)] \times \frac{1}{2\hbar^2\epsilon_0 c}\int d\nu I_q(\nu,\mathbf{r},t)\Phi_{JJ'}(\nu) \quad (14)$$

for the upper Zeeman levels and

$$\frac{\partial}{\partial t}n_{J'M'}(\mathbf{r},t) = r_{J'M'}(\mathbf{r},t) - \Gamma_{J'M'}(\mathbf{r},t)n_{J'M'}(\mathbf{r},t) + \sum_{q=\pm 1}\langle JM'+q|d_q|J'M'\rangle^2 \times [n_{JM'+q}(\mathbf{r},t) - n_{J'M'}(\mathbf{r},t)] \times \frac{1}{2\hbar^2\epsilon_0 c}\int d\nu I_q(\nu,\mathbf{r},t)\Phi_{JJ'}(\nu) \quad (15)$$

for the lower Zeeman levels. In the above equations, the n's are fractional populations defined by $n_{JM}=\langle JM|\rho|JM\rangle$. The r and Γ coefficients arise from all populating and depopulating processes, except those of absorption and induced emission. The last contribution in both equations represent the effect of the x-ray beam on the Zeeman level populations.

The radiative transfer and the whole set of population equations are solved consistently. The intervals $[s_{i-1},s_i]$ are taken sufficiently small, so that gain and emissivity can be assumed homogeneous in each one of them. We then have $G=G_i$ and $j=j_i$ for s between s_{i-1} and s_i. The equation of transfer is then easily solved, giving the intensity at a point M such that $M_0M=s$, where M_0 is the point from which the ray is launched [see Eq. (7)].

In Fig. 3 we plot the integrated intensity of the XRL beam as a function of distance from the target and time, at exit from plasma, for a propagation length of 5 mm. The Maxwell-Bloch calculation requires much larger calculation time than the first approach, and then has to be restricted to smaller sets of rays. The intensity values are three orders of magnitude smaller than with the first approach. These values are more reasonable and show the importance of accounting properly for the interaction between the XRL field and the amplifying medium. Rays launched at time $t=T_{\text{gain}}+2$ ps yield the largest intensity. The corresponding beam exits the plasma at a distance from target surface in the 40–45-μm range, which is in agreement with experiment.

The intensity of saturation obtained by the Maxwell-Bloch and EHYBRID codes is plotted in Fig. 4.

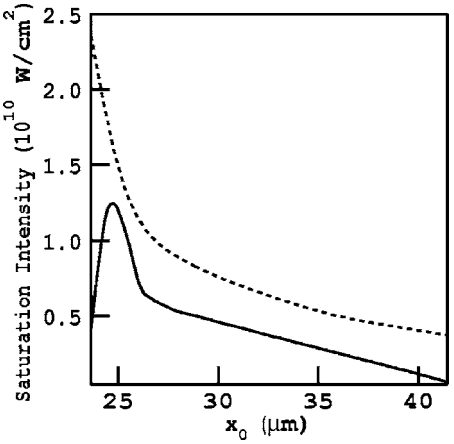

FIG. 4. Intensity of saturation calculated by EHYBRID (dot curve) and Maxwell-Bloch (solid curve) codes, vs distance to target surface, at time T_{gain}.

IV. COMPARISONS

A. Calculated gains

Figure 5 shows the variation of gain with propagation length for rays launched at various distances from the target surface. The comparison of the small-signal gain given by EHYBRID with the gain obtained by our ray-trace code illustrates the effect of saturation. Moreover, a better treatment of saturation (with the Maxwell-Bloch approach) yields more realistic gains $\lesssim 150$ cm^{-1}. Comparison of both Maxwell-Bloch calculations (with and without refraction) clearly demonstrates that the dominant effect is saturation. The propagation length for which saturation is reached is less than 1 mm in all cases when one uses the ray-trace code with the simplified treatment of saturation, while the Maxwell-Bloch approach gives lengths ~ 2 mm. This value is more satisfactory since most experiments on the Ni-like Ag line measure a length of 3 mm (see, e.g., Ref. [4]).

B. Theory vs experiment

Although the codes we developed can be applied to any recent experiment, we concentrate here specifically on the RAL experiment where, to our knowledge, the shortest x-ray laser pulse has been demonstrated [5]. An ultrafast streak camera from Axis Photonique, with maximum resolution of 800 fs, was coupled with a flat-field spectrometer. The measured pulse duration was 1.9 ± 0.7 ps. The setup provided spectral resolution in a narrow spectral range around the Ni-like $4d-4p$ line at 13.9 nm, and temporal resolution. Furthermore, the time-integrated signal level at a charge-coupled device (coupled to the same spectrometer) enabled the experimentalists to estimate the x-ray laser energy generated in the experiment to be in the range of $2-6$ μJ. The XRL peak was observed at the deflection angle of 5 mrad. The experimental deflection angle agrees with the angle at which the x-ray laser output peaks in our simulations.

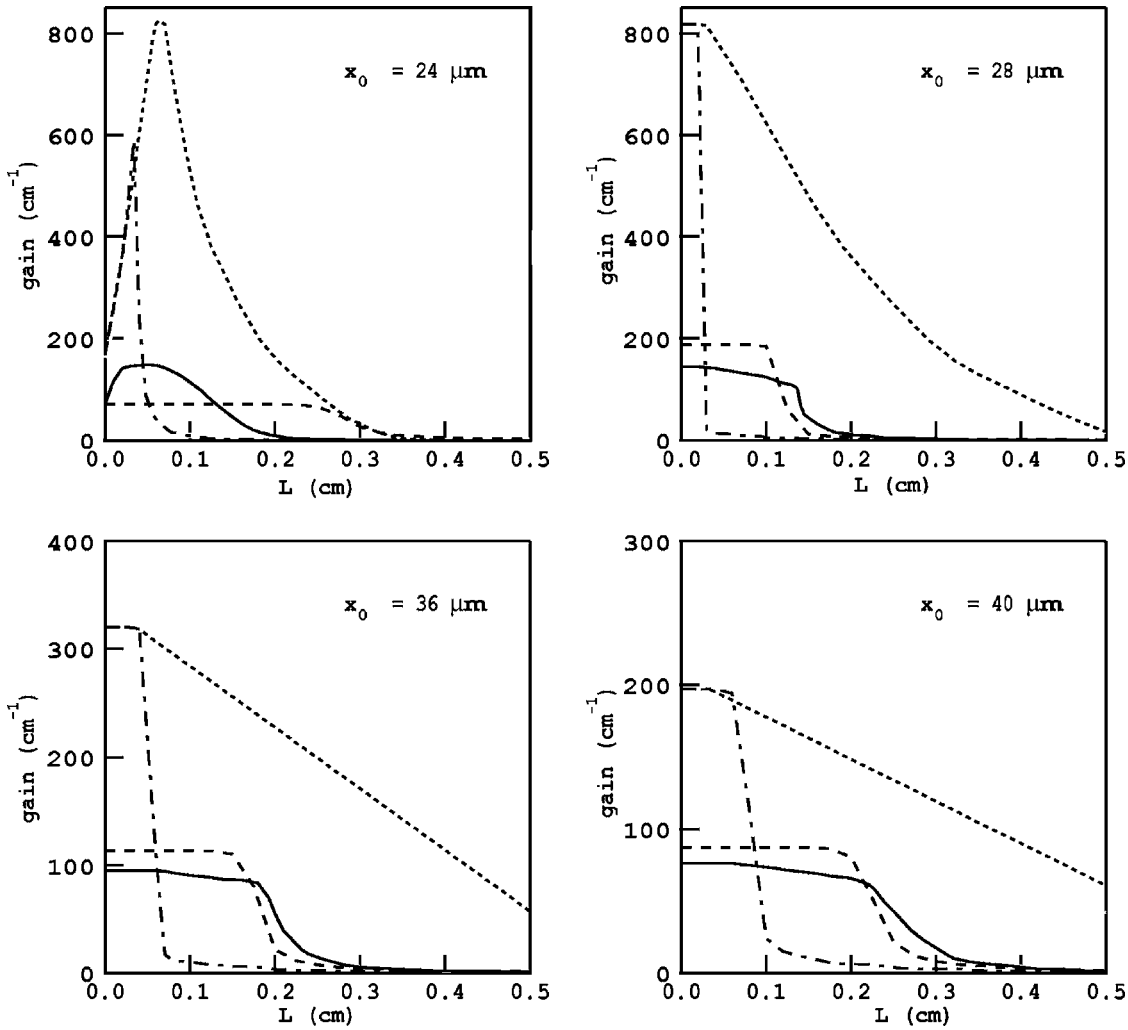

FIG. 5. Comparison of the local gains calculated by EHYBRID including refraction but not saturation effect: dot curve; ray-trace code (with saturation): dash-dot curve; Maxwell-Bloch approach without (with) refraction: dash (full) curve. The gain is plotted as a function of the propagation length L. The rays are launched at time T_{gain}, and for various distances x_0 from the target surface.

Although the source size was not measured during this experiment, consequent near-field experiments determined it to be in the range of 35–50 μm$\times$75–100 μm at the output from the plasma, peaking at 40–45 μm from the original target surface [27]. The ray-trace calculations show the source size to be 30×80 μm (see Fig. 2). Moreover, the x-ray laser peaks at 40 μm from the target surface (see Fig. 3).

Combining the measured pulse duration with the output transient x-ray laser energy, one obtains the output power of 1–3 MW. We can therefore infer the experimental output intensity to be a few 10^{10} W/cm^2, which agrees with the predicted intensity of 1.1×10^{10} W/cm^2 from our code (see Fig. 3).

The saturation length for Ag Ni-like XRL at 13.9 nm was measured in previous experiments. In the Limeil experiment (see Fig. 6 of Ref. [28]), the XRL saturated at $\sim$4 mm. The saturation length was even shorter in the following "LULI" experiment [29], where it was measured to be $<$3 mm. The simulation predicts a saturation length equal to 2 mm for the RAL case.

V. CONCLUDING REMARKS

We have modeled the RAL experiment on Ni-like Ag x-ray laser at wavelength 13.9 nm, in the transient pumping scheme. Two approaches were investigated. In the first one we have used a ray-trace code designed as a postprocessor of the hydroatomic code EHYBRID. The modeling shows that the calculated XRL source size agrees fairly well with measurements. Moreover, the beam exits the plasma at a distance from the target surface $\sim$50 μm, in agreement with experiment. However, owing to the poor treatment of saturation, the intensity values of the output are unrealistic. We have then developed a second approach based on the Maxwell-Bloch formalism. Refraction is also taken into account. The XRL intensity is much lower than in the first approach, typically three orders of magnitude lower. At saturation, the intensity of the output is close to 10^{10} W/cm^2, in good agreement with experiment. Concerning the distance to target at which the XRL beam exits the plasma, the agreement with experiment is even better than with the previous approach. The measured observables in the near-field of XRLs, within

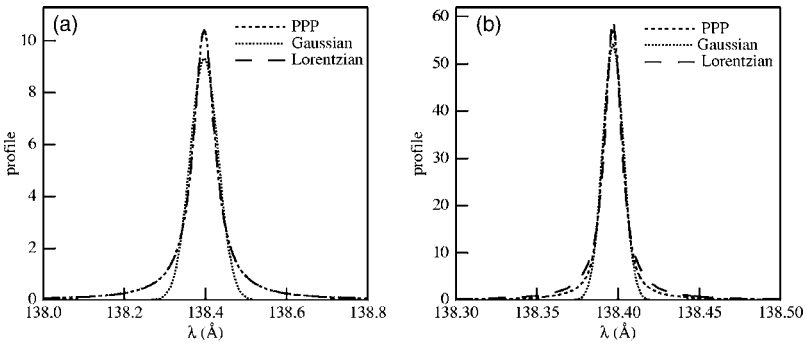

FIG. 6. Line profile calculated by the PPP code, at time T_{gain}. Also represented are the Lorentzian and Gaussian profiles: (a) near the target surface, with $n_e=2\times10^{21}$ cm^{-3}, $T_e=65$ eV, and $T_i=33$ eV; (b) in the region of peak gain, where $n_e=4.4\times10^{20}$ cm^{-3}, $T_e=1170$ eV, and $T_i=75$ eV.

the limitation of 1.5D hydrocode, as well as the output laser power, are well predicted by the new Maxwell-Bloch code.

Our description of the lateral expansion, using a Gaussian profile for electron density, has to be improved. In fact a 2D hydrocode would be preferable to the 1.5D code EHYBRID. This is an important issue to be addressed in future modeling of experiments.

ACKNOWLEDGMENTS

We are grateful to G. J. Pert (York University) for providing the EHYBRID code, and to J.-C. Gauthier (CELIA, Université Bordeaux I) who calculated the electron-ion collision cross sections with the HULLAC code.

APPENDIX

The PPP line-shape code [30] allows us to check that the Voigt profile, used in our calculations, is a good approximation for the investigated line. In fact, PPP calculations show that ion Stark broadening is negligible near the target surface, at high densities, as well as in the amplification region (densities $\sim10^{20}$ cm^{-3}). Figure 6(a) shows the PPP line shape at a distance of 22 μm from the target surface, where electron density $n_e=2\times10^{21}$ cm^{-3}, electron temperature $T_e=65$ eV, and ion temperature $T_i=33$ eV. The average ion charge is 9.24, and the proportion of Ni-like ions is very small. The PPP profile is Lorentzian, showing that electron broadening plays an important role, compared to Doppler broadening. Figure 6(b) represents the PPP profile obtained at a distance of 28 μm from the target surface, in the region where the gain reaches its maximum. In this case, we have $n_e=4.4\times10^{20}$ cm^{-3}, $T_e=1170$ eV, and $T_i=75$ eV. The average ion charge is now 18.7, and Ni-like ions are abundant. Due to the increase (decrease) of ion temperature (electron density), Doppler broadening is increased by a small amount. In both cases, electron impact broadening plays an important role.

[1] B. Rus, A. Carillon, P. Dhez, P. Jaeglé, G. Jamelot, A. Klisnick, M. Nantel, and Ph. Zeitoun, Phys. Rev. A **55**, 3858 (1997).
[2] J. Zhang, A. G. MacPhee, J. Lin, E. Wolfrum, R. F. Smith, C. Danon, M. H. Key, C. L. S. Lewis, D. Neely, J. Nilsen, G. J. Pert, G. J. Tallents, and J. S. Wark, Science **276**, 1097 (1997).
[3] P. V. Nickles, V. N. Shlyaptsev, M. Kalachnikov, M. Schnürer, I. Will, and W. Sandner, Phys. Rev. Lett. **78**, 2748 (1997).
[4] G. J. Tallents, J. Y. Lin, J. Zhang, A. Behjat, A. Demir, M. M. Güzegöz, C. L. S. Lewis, A. MacPhee, D. Neely, G. J. Pert, R. Smith, J. S. Wark, P. J. Warwick, and E. Wolfrum, in *Applications of High Field and Short Wavelengths Sources*, OSA Technical Digest Series, p. 59, edited by L. DiMauro, M. Murnane, and A. L'Huillier (Optical Society of America, Washington, DC, 1997).
[5] A. Klisnick, J. Kuba, D. Ros, R. Smith, G. Jamelot, C. Chenais-Popovics, R. Keenan, S. J. Topping, C. L. S. Lewis, F. Strati, G. J. Tallents, D. Neely, R. Clarke, J. Collier, A. G. MacPhee, F. Bortolotto, P. V. Nickles, and K. A. Janulewicz, Phys. Rev. A **65**, 033810 (2002).
[6] J. Nilsen and J. Dunn, Proc. SPIE **4505**, 100 (2001).
[7] J. Kuba, R. F. Smith, D. Benredjem, C. Möller, L. Upcraft, R. King, A. Klisnick, L. Drška, G. J. Pert, and J.-C. Gauthier, J. Opt. Soc. Am. B **20**, 208 (2003).
[8] F. Yan, J. Zhang, X. Lu, and J. Y. Zhong, Phys. Plasmas **11**, 3380 (2004).
[9] G. J. Pert, J. Fluid Mech. **131**, 401 (1983).
[10] R. A. London, Phys. Fluids **31**, 184 (1988).
[11] B. Rus, Inst. Phys. Conf. Ser. **159**, 119 (1999).
[12] J. L. A. Chilla and J. J. Rocca, J. Opt. Soc. Am. B **13**, 2841 (1996).
[13] J. Kuba, D. Benredjem, C. Möller, and L. Drska, J. Opt. Soc. Am. B **20**, 609 (2003).
[14] V. N. Shlyaptsev, J. J. Rocca, M. P. Kalachnikov, P. V. Nickles, W. Sandner, A. L. Osterheld, J. Dunn, and D. C. Eder, Proc. SPIE **3156**, 193 (1997).
[15] L. B. Golden, R. E. H. Clark, S. J. Goett, and D. H. Sampson, Astrophys. J., Suppl. Ser. **45**, 603 (1981).
[16] H. R. Griem, *Plasma Spectroscopy* (McGraw-Hill, New York, 1964).
[17] L. Spitzer, *Physics of Fully Ionized Gases* (Interscience, New York, 1962).
[18] I. P. Grant, Adv. Phys. **19**, 747 (1970).
[19] A. Bar-Shalom, M. Klapisch, and J. Oreg, J. Quant. Spectrosc. Radiat. Transf. **71**, 169 (2001).
[20] W. L. van Wyngaarden, K. Bhadra, and R. J. W. Henry, Phys.

Rev. A **20**, 1409 (1979).
[21] *Handbook of Mathematical Functions* edited by M. Abramowitz and I. A. Stegun (Dover, New York, 1970).
[22] D. Atwood, *Soft X-rays and Extreme Ultraviolet Radiation: Principles and Applications* (Cambridge University Press, Cambridge, England, 1999).
[23] M. Born and E. Wolf, *Principles of Optics*, 7th Edition (Cambridge University Press, Cambridge, England, 1999).
[24] G. Hazak and A. Bar-Shalom, Phys. Rev. A **38**, 1300 (1988).
[25] D. Benredjem, A. Sureau, B. Rus, and C. Möller, Phys. Rev. A **56**, 5152 (1997).
[26] D. Benredjem, C. Mossé, S. Ferri, B. Talin, and C. Möller, in *Proceedings of the 16th International Conference on Spectral Line Shapes*, edited by C. A. Back, AIP Conf. Proc. No. 645 (AIP, Melville, NY, 2002), p. 445.
[27] D. Ros, A. Klisnick, D. Joyeux, D. Phalippou, O. Guilbaud, J. Kuba, A. Carillon, G. Jamelot, R. F. Smith, M. Edwards, F. Strati, G. J. Tallents, H. Daido, H. Tang, P. Neumeyer, D. Ursescu, T. Kühl, J.-C. Chanteloup, and K. Bouhouch, in *8th International Conference on X-Ray Lasers, Aspen 2002*, edited by J. J. Rocca, J. Dunn, and S. Suckewer, AIP Conf. Proc. No. 641 (AIP, Melville, NY, 2002), p. 69.
[28] J. Kuba, A. Klisnick, D. Ros, P. Fourcade, G. Jamelot, J.-L. Miquel, N. Blanchot, and J.-F. Wyart, Phys. Rev. A **62**, 043808 (2000).
[29] O. Guilbaud, M. Edwards, A. Klisnick, D. Ros, G. Jamelot, D. Joyeux, D. Phalippou, H. Tang, P. Neumayer, D. Ursescu, G. J. Tallents, T. Kühl, K. Cassou, K. Bouhouch, M. Kado, M. Nishikino, K. Sukegawa, M. Kishimoto, M. Ishino. K. Nagashima, H. Daido, W. Seelig, S. Borneis, E. Gaul, W. Geithner, C. Häfner, and P. Wiewior, Proc. SPIE **5197**, 17 (2003).
[30] B. Talin, A. Calisti, L. Godbert, R. Stamm, R. W. Lee, and L. Klein, Phys. Rev. A **51**, 1918 (1995).